Facility scale detection and quantification of gas flaring using imaging spectrometers

Jinsol Kim*, Daniel H. Cusworth, Bradley M. Conrad, and Riley M. Duren

Carbon Mapper, Pasadena, CA, USA
*jinsol@carbonmapper.org

Abstract

Globally, over 140 billion cubic meters of natural gas are flared each year, according to the VIIRS Nightfire (VNF) data product derived from satellite observations by the Visible Infrared Imaging Radiometer Suite (VIIRS), the most widely used instrument for global flare monitoring. Although VIIRS routinely tracks global flaring activity through nighttime observations, its coarse spatial resolution limits the ability to attribute flares to specific facilities or operators. Here, we present flare detection and quantification using high spatial resolution imaging spectrometers. We demonstrate that NASA's Earth Surface Mineral Dust Source Investigation (EMIT) is capable of detecting flares at individual flare stacks with a probability of detection (POD) comparable to that of VIIRS. We further attribute the detected flare stacks in the Permian Basin during 2023 to individual operators and evaluate EMIT's potential to estimate annual flared gas volumes at the operator level. We find good correspondence between the EMIT observed radiant heat values and reported annual flared gas volume on the operator level. Despite limited temporal sampling relative to VIIRS, EMIT achieves accuracy comparable to VIIRS-based annual flaring estimates, while providing operator level attribution. This highlights the value of high-resolution imaging spectrometers in regulatory and mitigation efforts by adding insights at the operator level that can complement existing VIIRS observations, enabling more comprehensive flare monitoring and analysis.

Synopsis. In this study, we demonstrate for the first time the capability of a spaceborne imaging spectrometer, EMIT, to detect and quantify flaring activity at the level of individual flare stacks. We show that annual operator-level flared gas volumes can be estimated from EMIT-quantified flaring activity with accuracy comparable to that of widely used global monitoring systems like VIIRS. The methods and workflows developed here are directly transferable to other similar imaging spectrometer missions, such as Tanager-1, EnMAP, and PRISMA.

Keyword. EMIT, imaging spectrometer, oil and gas, methane, flaring, flared gas volumes, facility scale, operator level

1 Introduction

Every year, more than 140 billion cubic meters (bcm) of natural gas are flared globally, often for reasons related to safety, infrastructure limitations, or economic considerations[1]. Generally flaring is preferred over venting due to the effective reduction in carbon dioxide (CO_2)-equivalent emissions afforded by combustion. However, flaring still has significant environmental and public health impacts, releasing carbon dioxide (CO_2) and black carbon through combustion. Additionally, methane, volatile organic compounds, and potentially chlorinated hydrocarbons are

emitted due to incomplete combustion[2]. In 2024, flaring is estimated to have generated 389 million tons of carbon dioxide equivalent (CO_2e), including 46 million tons CO_2e from methane emission[3], which is likely underestimated due to the optimistic assumption of a 98% CH_4 destruction efficiency[4]. Flaring is not only a significant source of pollution but also represents a substantial waste of valuable natural resources. Consequently, monitoring gas flaring has been used as a proxy for tracking fossil fuel production activities, evaluating their effects on climate and public health, and enabling and confirming mitigation.

Global flaring activity is most commonly monitored and reported using the Visible Infrared Imaging Radiometer Suite (VIIRS) Nightfire (VNF) dataset derived from space-based observations[5]. VIIRS is mounted on three satellites (Suomi NPP, NOAA-20, and NOAA-21), which are separated in time and space on orbit, enabling extensive global coverage at 750 m spatial resolution. Each satellite overpasses a single location twice a day providing six observations per day (nominally three during nighttime) with VIIRS. The detection and quantification of flare characteristics, such as temperature, size, and radiant heat, are achieved using nine infrared (IR) spectral bands in multispectral nighttime observations[6]. At night, in the absence of sunlight, enhanced radiance is observed above the sensor noise in the near-infrared (NIR) and shortwave infrared (SWIR) bands of VIIRS in pixels containing IR emitters, such as biomass burning and gas flaring. Global flared gas volume is estimated using radiant heat quantified from VIIRS using a linear relationship found between observed radiant heat and reported flared gas volume at national level[7]. Recently, an improved calibration method based on the controlled experiments was reported, and a subsequent reprocessing effort was announced[8]. However, in the context of methane regulation, mitigation, and more-broadly measurement, reporting, and verification (MRV) efforts, VIIRS has limited facility-scale effectiveness. The coarse spatial resolution inherently aggregates closely located flares and may preclude attribution of observed flare(s) to a single facility and operator, particularly in the U.S.[9]. Zhizhin et al.[10] proposed a new method based on a multiyear database of detected flares to address this issue. Recently, multispectral instruments such as Sentinel-2 (10 – 60 m spatial resolution) and Landsat-8 (10 – 100 m spatial resolution) have been used to detect flares[11,12]. While they demonstrate effective detection capabilities for small flares, their applications has been limited to detection rather than quantification due to the challenge of separating daytime solar-reflected radiance from the IR emission.

Imaging spectrometers that measure solar backscattered radiance from visible to infrared (400 to 2500 nm) at 5-15 nm spectral resolution have been used to detect and quantify daytime fire characteristics[13] by isolating blackbody emission from solar backscattered radiance. In this paper, we apply this approach to the NASA Earth Surface Mineral Dust Source Investigation (EMIT) instrument[14], which is an imaging spectrometer onboard on the International Space Station collecting hyperspectral imagery at 60 m spatial resolution. We use EMIT data to assess flaring activity in the Permian Basin, which is one of the highest-producing oil and gas regions in the world; oil production in the Permian Basin has increased from 1.37 million barrels per day in 2013 to 5.94 million barrels per day in 2023, accounting for 46% of the US total oil production of 12.94 million barrels per day in 2023 (Energy Information Administration).

First, we compare EMIT flare observations in August of 2023 with VIIRS nighttime flare observations and coincident airborne under flights from the Global Airborne Observatory (GAO)[15]. This comparison allows us to

evaluate EMIT's flare detection and quantification performance, while also identifying the strengths and limitations of the instrument as compared to VIIRS. We demonstrate that EMIT's high spatial resolution enables the detection of individual flares at the facility level, which VIIRS is unable to resolve. Finally, using these EMIT observations as a case study, we assess the ability of spaceborne imaging spectrometers to estimate annual flared gas volumes at the operator level using observations in the Permian Basin during 2023, demonstrating the potential of high-resolution satellite data to inform operator-level flaring activity.

2 Materials and Methods

2.1 Data

We perform flare detection and quantification using imaging spectrometer data collected by EMIT and GAO. Both imaging spectrometers measure radiance across wavelengths of 400 to 2500 nm, with a spectral resolution of ~7 nm for EMIT and ~5 nm for GAO. EMIT images are generally 80 km by 80 km with ~60 m spatial resolution. The swath width and pixel size of GAO vary depending on the altitude of the aircraft. GAO data used in this study has a swath width of ~3 km and spatial resolution of ~5 m.

EMIT is a targeted imaging spectrometer acquiring data over selected regions during daytime overpasses when tasked. On August 20th and 24th, 2023, EMIT observed large areas of the Permian Basin. As detailed by Ayasse et al. (2025)[16], coincident GAO under flights were coordinated to compare the methane detection performance of the GAO and EMIT instruments. These experimental data also offer an opportunity to compare flaring detection and quantification performance in this globally critical oil and as region.

In addition, we compare EMIT observations to nighttime flare data collected by VIIRS. VIIRS instruments operate on sun-synchronous satellites at ~830 km altitude with a spatial resolution of ~750 m, whereas EMIT is mounted on the International Space Station at a lower altitude of ~400 km, providing a much finer spatial resolution of ~60 m. We use VIIRS Nightfire (VNF) data product V30-ez for VIIRS in this study. V30-ez is a simplified dataset providing a subset of the more comprehensive V30 flare detection data excluding the detections surrounding the IR emitters caused by the atmospheric scatter and duplicate detections resulting from the overlap of scan lines[6]. While Zhizhin et al.[10] reported that including some of these edge pixels can improve flare quantification, the V30 (sum of all pixels) and V30-ez (local maximum only) approaches exhibit similar coefficients of determination values (see Table 2 in Zhizhin et al., 2025). Note that V30 may overestimate and V30-ez may underestimate the flare activity. We use V30-ez for its simplicity and ease of processing. We gather flare observations from the nights before and after EMIT and GAO observations, restricting the data to flares within the boundaries of the EMIT and GAO overpasses. Six VIIRS observations (two from each of three satellites) were processed by grouping flares detected within 1500 m of one another into a single flare location, considering VIIRS's spatial resolution of 750 m. Flare characteristics, including temperature, size, and radiant heat, are then averaged across grouped detections.

2.2 Flare detection and quantification method

Enhanced radiance from flaring activity have been observed in SWIR bands. Enhancements from blackbody emitters like gas flares follow Planck's equation describing the spectral radiance ($\beta(\lambda, T)$ [W sr^{-1} m^{-3}]) emitted at each wavelength (λ [m]) from an object at certain temperature (T [K]):

$$\beta(\lambda, T) = \frac{2hc^2}{\lambda^5} \frac{1}{e^{hc/\lambda k_B T} - 1} \quad (1)$$

where k_B is the Boltzmann constant [J K^{-1}], h is the Planck constant [J s], and c is the speed of light [m s^{-1}]. Flare observations from VIIRS show gas flare temperatures ranging from 1500 K to 2000 K with most flares clustered between 1700 K and 1800 K [7]. At a temperature of 1800 K, a blackbody emitter exhibits enhanced radiance in SWIR bands in imaging spectrometer data with a peak radiance near 1.6 µm, as described by Planck's and Wien's Displacement laws. This enhanced radiance can interfere with algorithms that rely on these wavelengths, such as those used for retrieving methane and carbon dioxide concentrations. For example, to minimize methane concentration retrieval artifacts, Cusworth et al. (2021) identified and removed potential corrupted flare pixels by setting a saturation threshold of 6 µW cm^{-2} sr^{-1} nm^{-1} in the 2100 nm band.

In this study, we used an improved flare detection method designed to identify smaller or lower-radiance flares more reliably, while minimizing false positives. We first calculate the average radiance in the 2400–2500 nm range ($L_{2400-2500}$ [µW cm^{-2} sr^{-1} nm^{-1}]), which was chosen after testing several ranges in the SWIR bands. Flare pixels exhibit high $L_{2400-2500}$ values, however, rooftops with high albedo also show elevated radiance in this range. To isolate flare pixels from rooftop pixels, we calculate a flare detection index defined as high $L_{2400-2500}$ values divided by maximum radiance between 400 and 750 nm in visible (VIS) bands. This index is designed based on the fact that high-albedo surfaces tend to exhibit strong radiance in the VIS range, whereas flare pixels are not as enhanced in the VIS range as described by Planck's law, resulting in large index values in flare pixels and small in rooftop pixels. Pixels with both $L_{2400-2500}$ and flare detection index above the 99.99th percentile of each EMIT scene and the 99.999th percentile of each GAO scene are identified as flare pixels. To ensure spatial continuity of detected flare regions, small gaps between adjacent flare pixels are filled and then connected pixels are grouped to form a flare observation, a group of flare pixels from one flaring source. To reduce false positives, we applied an additional filtering step: Each connected component (i.e., flare candidate) was evaluated for its maximum flare detection index. If the maximum flare detection index of a candidate was below a stricter threshold (0.005 above 99.99th percentile for EMIT and 0.05 above 99.999th percentile for GAO), the flare candidate was removed. Cloud pixels flagged in the Level 2A mask product of EMIT are excluded. Lastly, as an additional quality check, we compare candidate flares with visible imagery from Google Earth to confirm visual evidence of a flare stack.

Observed radiance is assumed to be the sum of solar backscattered radiance from the background and emitted radiance from flares. We use multiple endmember spectral mixing approach to model the background radiance following Dennison et al. (2011). This approach has been validated and applied to both simulated and observed spectral datasets of fire[13,17], exhibiting the same behavior as flares but over a lower temperature range[18]. A K-means clustering algorithm is used to define four endmembers radiance, which is the mean radiance of each cluster, using

only non-flare pixels inside the square box surrounding the flare pixels. We fit the observed radiance to the model radiance (L_λ) composed of four background endmember radiance (L_{ib}) and IR emitter radiance (L_f):

$$L_\lambda = \sum_{i=1}^{n} f_{ib} L_{ib} + \varepsilon L_f \quad (2)$$

where f_{ib}, fractional contribution of each background endmember radiance, sums to one and ε is the emissivity. L_f follows Planck's equation (eq 1) with necessary unit conversion to μW cm^{-2} sr^{-1} nm^{-1}. We perform the fitting for each temperature in the range of 500 to 3000 K with increments of 50 K, only using the bands not affected by absorption caused by water vapor, CH_4 and CO_2 (yellow dots on the right panel of Figure 1). Saturated bands that were interpolated and flagged in the Level 2A mask product of EMIT are excluded. The temperature with the minimum root mean square error (RMSE) is determined as the temperature of the flare and the optimum ε value found at that temperature is determined as the emissivity of the flare (vertical dashed line on the left panel of Figure 1). While the emissivity used by VIIRS represents an effective emissivity that accounts for sub-pixel flare sizes, the emissivity retrieved from EMIT more closely approximates the true emissivity, as EMIT's finer spatial resolution allows capturing the spatial extent of the flare more completely.

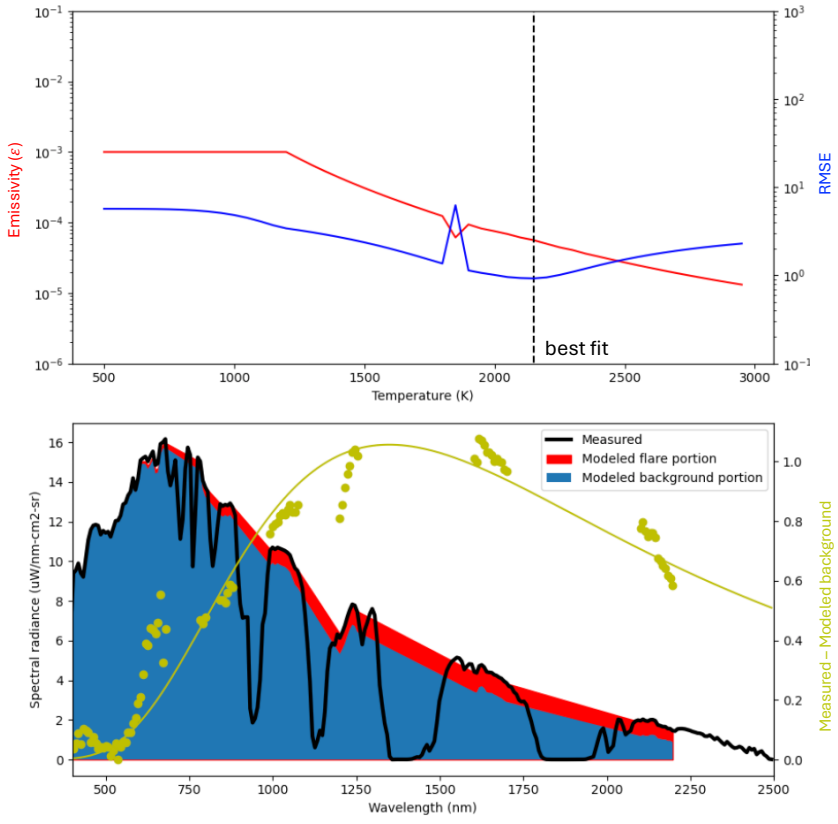

Figure 1. Example fitting result for a flare pixel. The left panel shows the emissivity and RMSE derived for each temperature between 500K and 3000K. The right panel shows the fitting result at the best fit, corresponding to the minimum RMSE. Measured spectral radiance, modeled flare portion and modeled background portion is plotted on

the left axis. The measured radiance, with the modeled background subtracted, is plotted on the right axis with dots representing the bands used for the fitting, excluding the band affected by strong absorptions, and solid line representing the fitted Planck curve.

The fitting described above is performed on a pixel-by-pixel basis for each flare observation. Identical background endmember radiances are applied to all pixels that comprise a given flare observation. In a flare observation, we perform the fitting starting from a pixel with largest $L_{2400-2500}$ to smallest. For the largest radiance pixel, we constrain ε to be between $10^{-6} - 10^{-3}$ for EMIT and $10^{-4} - 10^{-1}$ for GAO. The lower bound is imposed to account for cases in which radiance saturation, excluded from the fitting, occurs in bands shortward of the true radiance peak. Without this constraint, the fitting can yield unrealistically high temperature estimates. When fitting the next largest radiance pixel, we constrain ε and T to be smaller than the previous pixel. Derived ε and T of all the pixels are then used to calculate the source area and radiant heat of a flare. The source area is defined as the size of the source assuming a black body with emissivity of one, which is calculated as

$$Source\ Area = \sum_{j=1}^{N} A\varepsilon_j \quad (2)$$

where A is the pixel size and N is the number of pixels in a flare observation. Radiant heat, the amount of energy carried by the radiation, is calculated using Stefan-Boltzmann's Law following

$$Radiant\ Heat\ (RH) = \sum_{j=1}^{N} A\varepsilon_j \cdot \sigma \cdot T^4 \quad (3)$$

where σ is Stefan-Boltzmann constant [W m^{-2} K^{-4}].

3 Results and Discussion

3.1 Performance of EMIT-derived flare detection and quantification

The top row of Figure 2 presents the flare detections by EMIT (red circles) and GAO (green circles) during the coordinated coincident airborne under flights. Within the overlapping overpasses between EMIT and GAO, EMIT detected 20 flares (8 on August 20 and 12 on August 24) among 137 GAO-detected flares (77 on August 20 and 60 on August 24), resulting in a detection rate of 15% for the GAO-detected flares. The time difference between coincident flare observations ranges from 1 minute to less than 2.5 hours. We find a strong correlation in RH values between EMIT and GAO for flares detected by both instruments (as shown in the bottom right panel of Figure 2). The three outliers in the lower RH range are likely caused by the variability in flaring at each source. EMIT missed flares can be primarily explained with lower RH (as shown in the bottom left panel of Figure 2). This corresponds to EMIT's lower sensitivity to emitted radiance compared to GAO, due to both its coarser spatial resolution and the greater sensor-to-target distance inherent to its spaceborne platform.

The top row of Figure 3 shows the flares detected by EMIT (red circles) and VIIRS (blue circles) within EMIT's overpasses of the Permian Basin. EMIT identified 96 flares on August 20 and 74 flares on August 24. Of these, 77 flares on August 20 and 59 flares on August 24 were spatially matched with VIIRS-detected flares. These correspond to 72 VIIRS flares on August 20 and 50 VIIRS flares on August 24, reflecting differences in spatial resolution and grouping between the two instruments. Additional detections occur in areas where multiple flare stacks are located in close proximity, making it difficult for VIIRS to distinguish individual flares. However, EMIT has the capability to resolve them with its finer spatial resolution and can more accurately determine the flare location, allowing it to be associated with a specific flare stack (see Figure 4). Correspondingly, the RH distribution in the bottom left panel of Figure 3 shows a higher range of RH values observed by VIIRS as a result of observing cluster of flares summing the RH of individual flares. EMIT detected lower-RH flares that VIIRS failed to capture due to the coarser spatial resolution. Consistently, we observe a strong correspondence in RH values between EMIT and VIIRS for flares detected by both instruments (as shown in the bottom right panel of Figure 3).

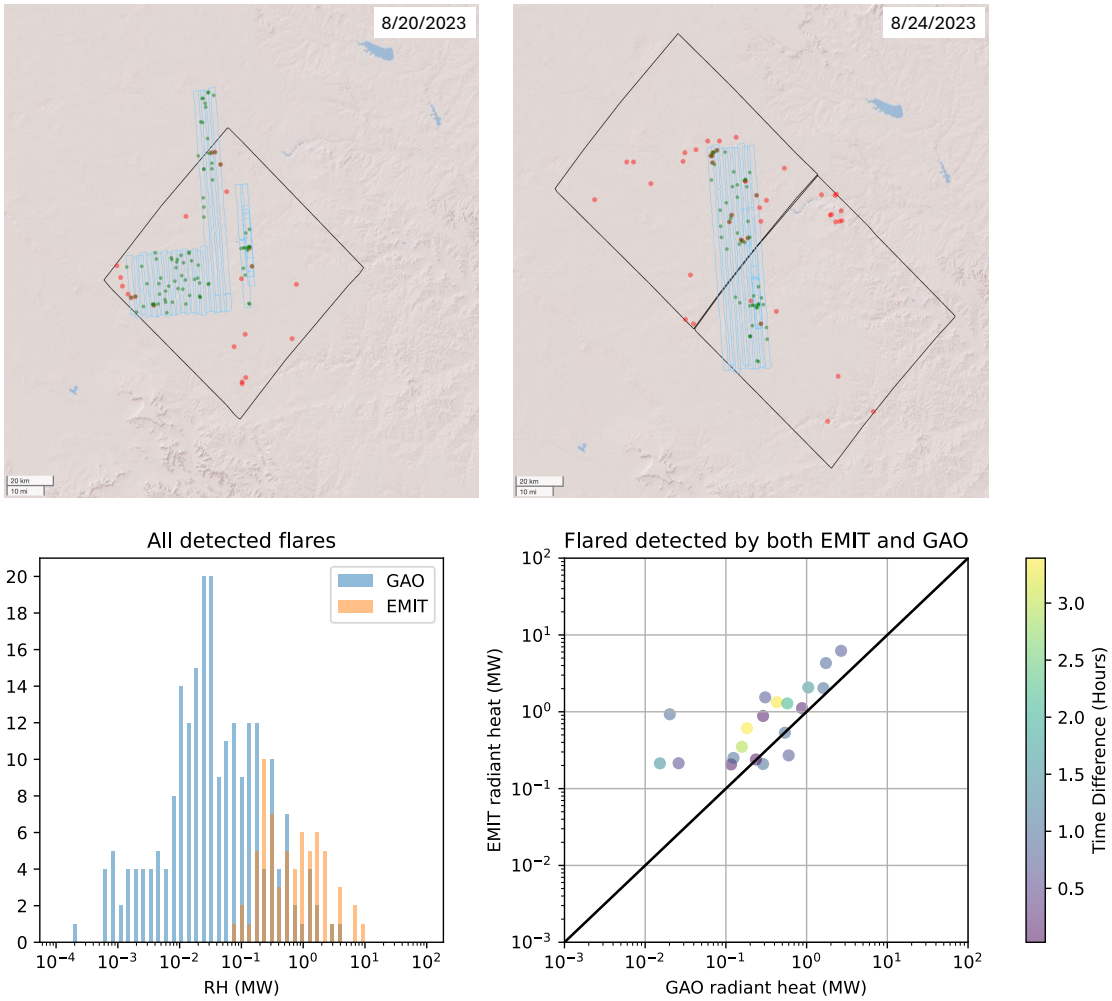

Figure 2. Top row shows the map of flares detected by EMIT (red circles) and GAO (green circles) on August 20th, 2023 (left panel) and August 24th, 2023 (right panel). The black line represents the EMIT overpass and the cyan line indicates the coverage of coincident airborne under flights by GAO. Bottom row shows histogram of RH values from the flares detected on August 20th and August 24th, 2023 (left panel), and RH comparison between EMIT and GAO for the flares detected by both instruments (right panel).

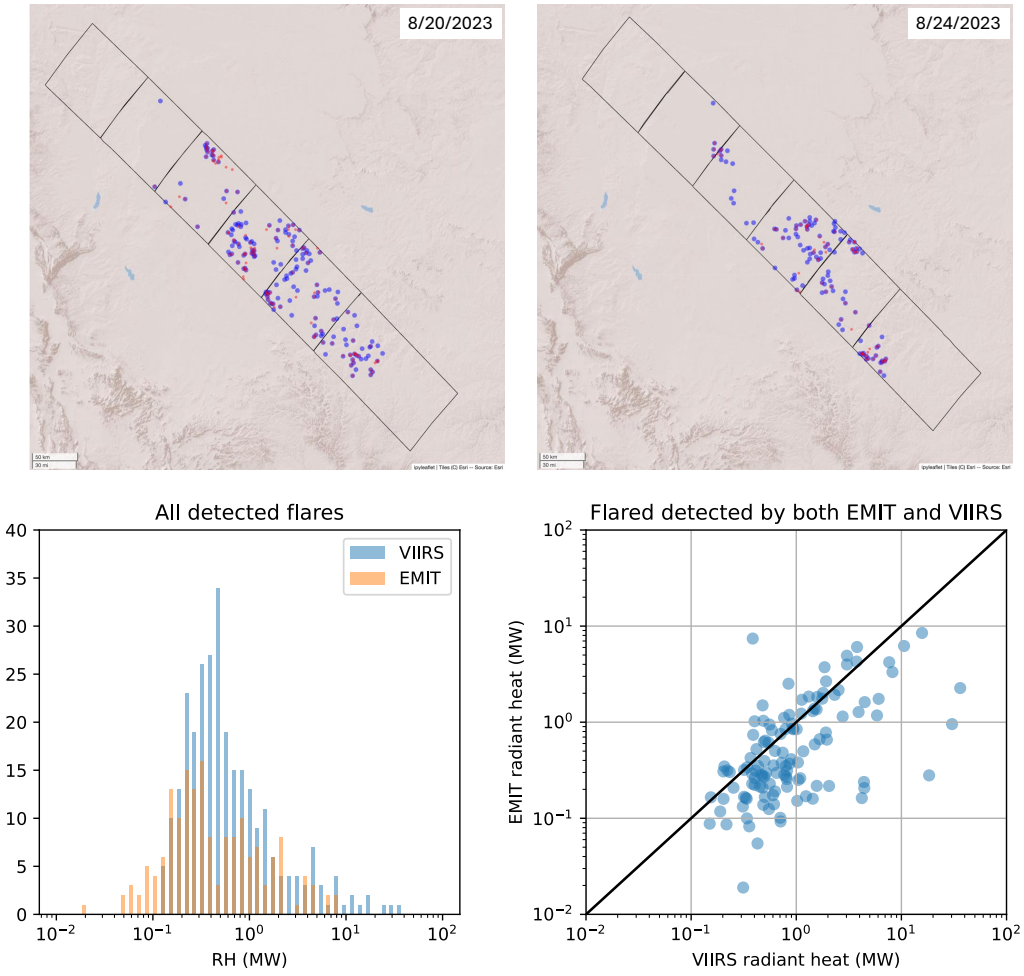

Figure 3. Top row shows the map of flared detected by EMIT (red circles) and VIIRS (blue circles) on August 20th, 2023 (left panel) and August 24th, 2023 (right panel) within the EMIT overpasses (black line). Bottom row shows histogram of RH values from the flares detected on August 20th and August 24th, 2023 (left panel), and RH comparison between EMIT and VIIRS for the flares detected by both instruments (right panel).

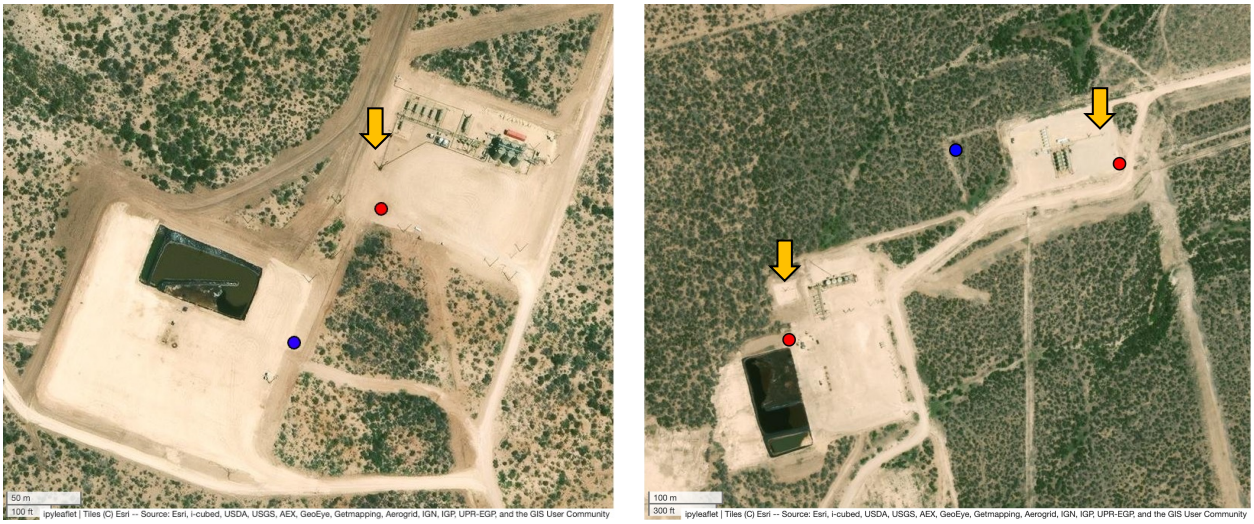

Figure 4. Example of flare detection displayed on visible imagery. Flares detected by EMIT are shown as red circles, VIIRS detections are shown as blue circles, and the flare stack locations are marked with arrows. The two flare stacks in the right panel are approximately 500 meters apart.

Overall, VIIRS detected more flares than EMIT, 167 flares on the 20th and 117 flares on the 24th, which is likely due to simplicity of VIIRS's night-time observations which are not affected by solar backscattered radiance as well as the operation of three satellites. Additionally, some of the discrepancy may be explained by temporal variability in flaring activity, where short-lived or intermittent flares active during nighttime when VIIRS overpasses may have been inactive during daytime when EMIT observations are collected. We also find flares detected by EMIT but missed by VIIRS, 19 flares on the 20th and 15 flares on the 24th, likely due to flares active during daytime and inactive during nighttime or heat emitted below the VIIRS detection limit.

The concept of probability of detection (POD) is commonly used to assess the performance of imaging spectrometers in detecting methane and carbon dioxide plumes[16,19,20]. POD describes how the likelihood of detection by an observing system varies with emission rate, generally decreasing at lower emission rate. POD can be applied for flare detection using RH describing the probability of detecting flares as a function of RH. We use coincident data (points marked in top panel of Figure 2) from EMIT and GAO to derive a POD model for EMIT flare detections. The lowest RH detected 0.0002 MW for GAO and 0.07 MW for EMIT. GAO's lower detection limit enables the compilation of a rich dataset comprising both detected and missed flares, which is essential for robust POD modeling. We use arctan model with RH as a predictor variable as in the following equation:

$$POD = \frac{\tan^{-1}\left(\frac{\pi}{2} \times \emptyset_1 \times RH^{\emptyset_2}\right)}{\pi/2} \quad (4)$$

Other variables, such as solar zenith angle and albedo, would also affect the detection, however, there was not enough variability in those variables in our constrained study region. Optimization of the coefficients $\emptyset_1$ and $\emptyset_2$ is performed by minimizing the l:

$$l = \sum_i -(D_i ln F_i + (1 - D_i) ln(1 - F_i)) \quad (5)$$

where D_i represents a successful detection (1) or a missed detection (0) and F_i represents POD model output from Eq (4) for each flare observation (i). We find $\emptyset_1$ of 0.615 and $\emptyset_2$ of 0.629 best explaining the flare detection performance of EMIT.

We find that flares with an RH of 0.06 MW have a 10% POD, while those with an RH of 20 MW have a 90% POD (see Figure 5). Our 10% POD at 0.06 MW is within the detection limit of VIIRS estimated in previous studies that range from 0.001 MW to 0.1 MW[9,21,22]. Detection limits reported in flared gas volumes (in $m^3\ yr^{-1}$) was converted to RH (MW) using the linear coefficient of 0.0274 ($m^3\ yr^{-1}\ MW^{-1}$)[7]. Compared to the latest reported VIIRS detection limit of approximately 0.2 MW[8], based on the most up-to-date calibration and conversion of flared gas volumes using the coefficient reported in the same study, EMIT demonstrates a lower detection limit.

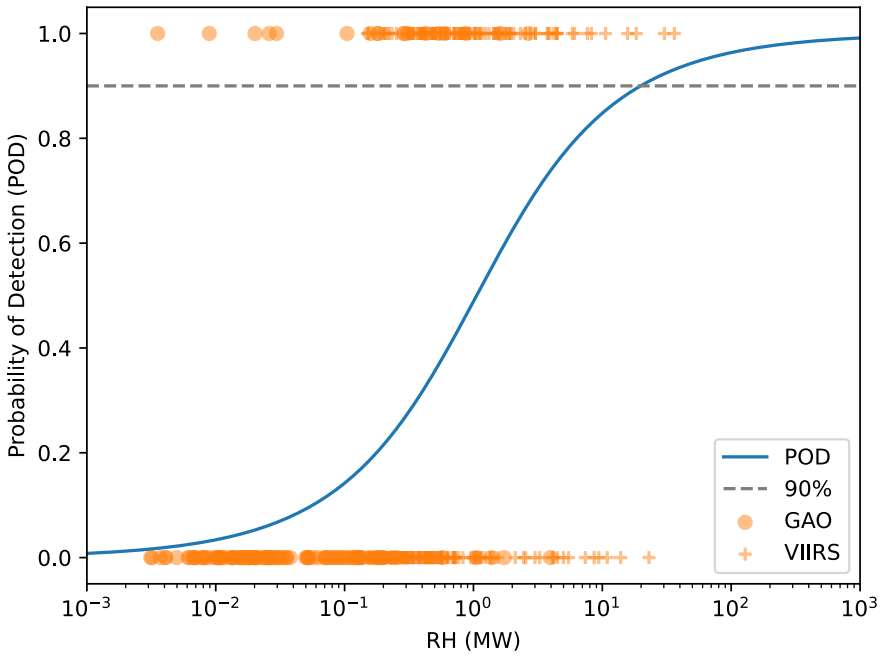

Figure 5. Probability of detection (POD) of flare activities for EMIT derived from flare detections by GAO. Points at zero represent flares missed by EMIT and points at one represent flares successfully detected by EMIT.

3.2 EMIT-derived flared gas volume at the operator level

We analyze all EMIT observations over the Permian Basin in 2023. In total, 233 scenes overpassed the region, with each scene capturing a portion of the basin. 99.98 % of the basin was observed at least once from EMIT. Overall, 1154 flares were observed from 802 flare stacks. Each flare stack was detected 1-5 times across an average of five overpasses. We use Rextag Energy DataLink (https://rextag.com/) to attribute each flare to an operator/owner, where possible. RH observations at each flare stack were first averaged, including non-detects as zero, and then summed for each company. We compare total RH emitted from each operator quantified from EMIT and flared gas volume reported in the U.S. EPA Greenhouse Gas Reporting Program (GHGRP) Subpart W. Since operators report emissions in metric tons of CO_2 rather than flared gas volume, we convert the reported CO_2 emissions to flared gas volume in billion cubic meters (bcm) assuming Permian Basin's gas composition values as provided in Table S2 of Plant et al. (2022) and combustion efficiency of 96.5 % following GHGRP reporting rules. Reported CO_2 emissions from "Associated Gas Venting and Flaring" as well as emissions from Tanks, Compressors, Completions/Workovers, Dehydrators, and Flare stacks were aggregated and used following procedures laid out in Flaring Accountability: Global Gas Flaring by Major Oil and Gas Companies and Their Partners (2024).

We find a linear relationship between the two explained with a coefficient of 0.02 ± 0.004 and r-squared of 0.68 ± 0.16 (see Figure 6). Mean and standard deviation of the coefficient and r-squared value was calculated via bootstrap. This coefficient, linking RH with flare volume, is consistent with values reported in previous studies, including 0.0274 reported by Elvidge et al. (2016)[7] and 0.0115 reported by Zhizhin et al. (2025)[8]. Note that this coefficient serves as a calibration factor and depends on the accuracy of RH quantification. Using this correlation, we estimate the flared gas volume of 3.85 ± 0.77 bcm in the Permian Basin using EMIT. The value of 3.66 bcm reported in the GHGRP is within this range.

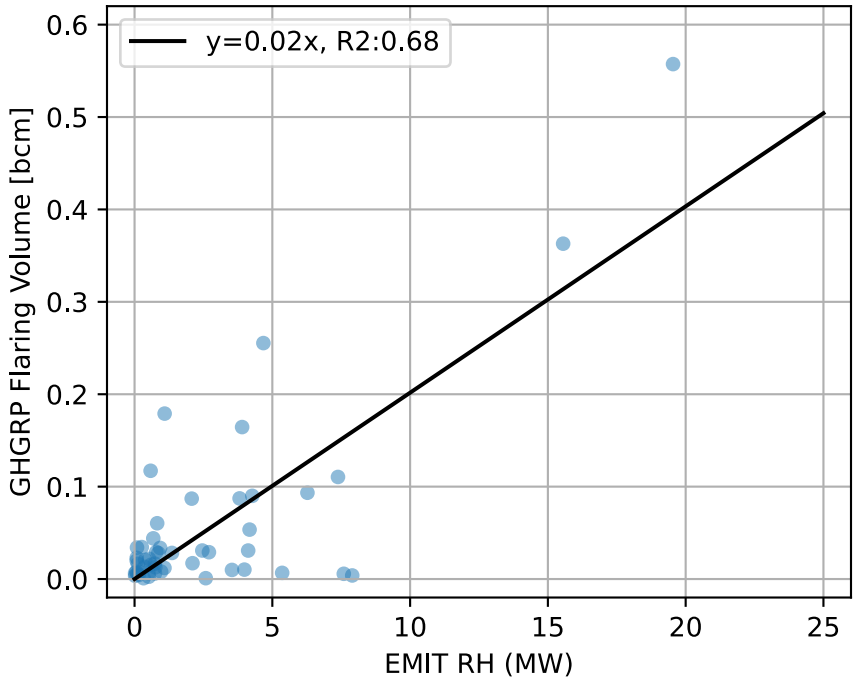

Figure 6. Correlation between EMIT RH and GHGRP flaring volume at the operator level. EMIT RH values are first averaged for each flare stack and then aggregated across all facilities operated by the same company.

We compare our estimation to World Bank's estimated annual volume from VIIRS[25]. VIIRS detected 1576 flare locations over the Permian Basins in 2023. Of these, EMIT detected 614 flare stacks corresponding to 528 VIIRS-observed flares. VIIRS estimated a total flared gas volume of 5.36 bcm over the Permian Basin. Among these totals, 3.50 bcm is observed by EMIT while 1.86 bcm is missed. These differences are primarily attributable to EMIT's limited temporal sampling, which tends to miss low-persistence (intermittent) flares but successfully captures high-persistence (continuous) sources (see Figure 7).

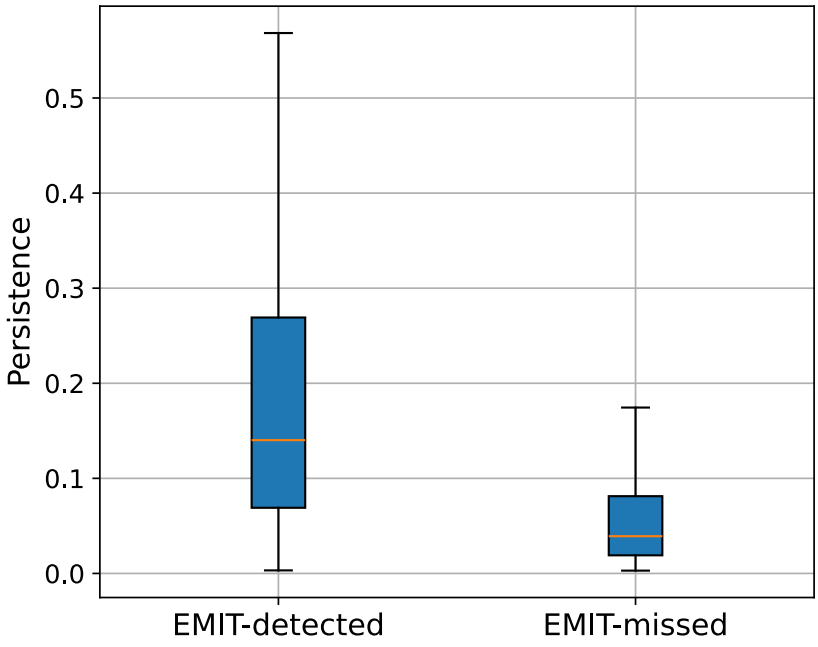

Figure 7. Distribution of flaring activity persistence for VIIRS flare stacks detected and missed by EMIT.

We assess the accuracy of EMIT based annual flaring volume estimates at operator level by comparing it to the reported volume in the GHGRP, following previous studies[22,24]. We find 61% of EMIT estimates within a half order of magnitude of reported volumes and 83% within a full order of magnitude (see Figure 8). The accuracy of EMIT-based flaring volume estimates is comparable to those derived from VIIRS, as assessed in Seymour et al. (2025)[22]. Despite EMIT's limitation in temporal sampling, its high spatial resolution enables operator-level flaring volume estimates with accuracy comparable to VIIRS. This underscores the value of spaceborne imaging spectrometers like EMIT for high-resolution, operator-specific flaring assessments and mitigation efforts. When considered alongside VIIRS's consistent global and temporal coverage, EMIT can contribute to more comprehensive flare monitoring and attribution.

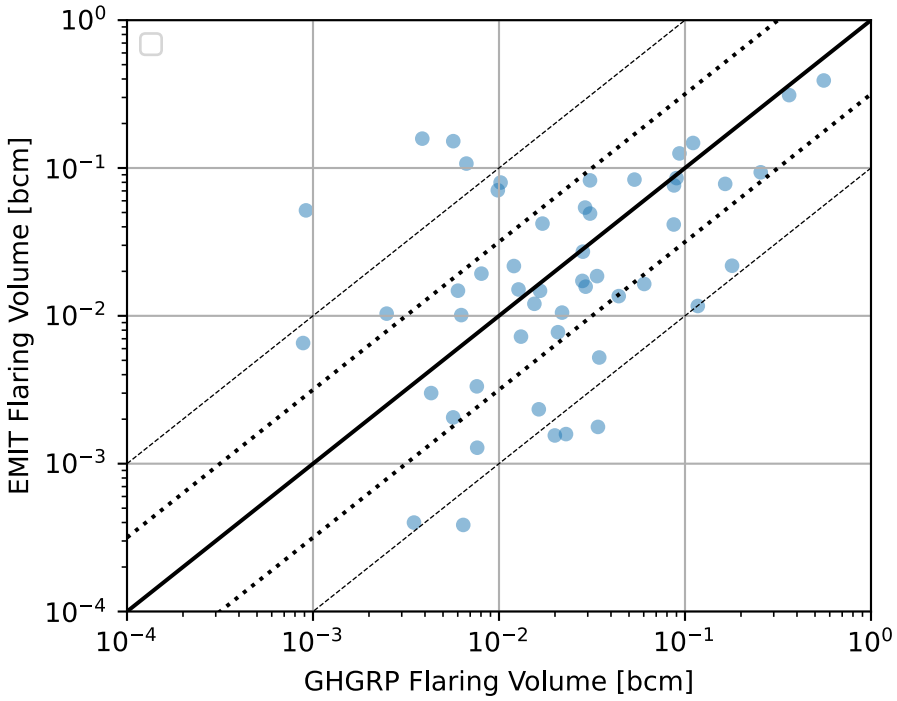

Figure 8. Log-log comparison between EMIT based flaring volume estimates and GHGRP flaring volume at the operator level. Solid line shows the 1:1 line, dotted line shows ± 0.5 order of magnitude lines, and dashed line shows ± 1 order of magnitude lines.

The algorithms and workflows described and demonstrated here with EMIT and GAO are directly attributable to similar remote imaging spectrometer missions (Tanager-1[26]; EnMAP[27]; PRISMA[28]), albeit with varying levels of sensitivity based on the performance of those sensors. Imaging spectrometers have been widely used for detecting and quantifying high-emitting point sources of CH_4[14,29–32] and CO_2[33–35]. Integrating these greenhouse gas emission datasets with flare activity datasets offers a unique opportunity to enhance our understanding of flare dynamics and their environmental impacts. This integration could facilitate the classification of flare stacks into categories such as fully combusting, partially combusting, unlit, and venting flares at the moment of observation, providing critical insights into their operational status. Furthermore, it allows for the direct quantification of methane removal efficiency, which is essential for evaluating combustion performance[36]. These insights are essential for developing targeted climate mitigation strategies and improving air quality management.

Acknowledgements

The Carbon Mapper team acknowledges the generous support of its philanthropic donors. We would like to thank the GAO (Global Airborne Observatory) team for flight operations. The GAO is managed by the Center for Global Discovery and Conservation Science at Arizona State University. The GAO is made possible by support from

private foundations, visionary individuals, and Arizona State University. Funding for flight operations and/or data analysis referenced in this paper was supported by the Grantham Foundation for the Protection of the Environment, Bloomberg Philanthropies, the High Tide Foundation, the California Air Resources Board (CARB), the University of Arizona, and Orbiting Carbon Observatory Science Team, and the NASA Carbon Monitoring System program

365

References

(1) *What is Gas Flaring?* https://www.worldbank.org/en/programs/gasflaringreduction/gas-flaring-explained (accessed 2024-11-21).

(2) Milani, Z. R.; Conrad, B. M.; Roth, C. S.; Johnson, M. R. Fence-Line Spectroscopic Measurements Suggest Carry-Over of Salt-Laden Aerosols into Flare Systems Is Common. *Environ. Sci. Technol. Lett.* **2023**, *10* (11). https://doi.org/10.1021/acs.estlett.3c00613.

(3) *Global Gas Flaring Tracker Report: 2025*; 2025. www.worldbank.org.

(4) Plant, G.; Kort, E. A.; Brandt, A. R.; Chen, Y.; Fordice, G.; Gorchov Negron, A. M.; Schwietzke, S.; Smith, M.; Zavala-Araiza, D. Inefficient and Unlit Natural Gas Flares Both Emit Large Quantities of Methane. *Science (1979).* **2022**, *377* (6614), 1566–1571. https://doi.org/10.1126/science.abq0385.

(5) Elvidge, C. D.; Zhizhin, M.; Hsu, F. C.; Baugh, K. E. VIIRS Nightfire: Satellite Pyrometry at Night. *Remote Sens. (Basel).* **2013**, *5* (9), 4423–4449. https://doi.org/10.3390/rs5094423.

(6) Elvidge, C. D.; Zhizhin, M.; Baugh, K.; Hsu, F. C.; Ghosh, T. Extending Nighttime Combustion Source Detection Limits with Short Wavelength VIIRS Data. *Remote Sens. (Basel).* **2019**, *11* (4). https://doi.org/10.3390/rs11040395.

(7) Elvidge, C. D.; Zhizhin, M.; Baugh, K.; Hsu, F. C.; Ghosh, T. Methods for Global Survey of Natural Gas Flaring from Visible Infrared Imaging Radiometer Suite Data. *Energies (Basel).* **2016**, *9* (1). https://doi.org/10.3390/en9010014.

(8) Zhizhin, M.; Elvidge, C. D.; Sparks, T.; Ghosh, T.; Bazilian, M.; Hsu, F. C. An Improved Calibration for Satellite Estimation of Flared Gas Volumes from VIIRS Nighttime Data. *Energies (Basel).* **2025**, *18* (17). https://doi.org/10.3390/en18174765.

(9) *Flaring Accountability: Global Gas Flaring by Major Oil and Gas Companies and Their Partners*; 2024. www.catf.us.

(10) Zhizhin, M.; Elvidge, C. D.; Ghosh, T.; Gleason, G.; Bazilian, M. VIIRS Nightfire Super-Resolution Method for Multiyear Cataloging of Natural Gas Flaring Sites: 2012-2025. *Remote Sens. (Basel).* **2026**, *18* (2), 314. https://doi.org/10.3390/rs18020314.

(11) Hu, C.; Zhang, X.; Xing, X.; Gao, Q. An Approach to Detect Gas Flaring Sites Using Sentinel-2 MSI and NOAA-20 VIIRS Images. *International Journal of Applied Earth Observation and Geoinformation* **2023**, *124*. https://doi.org/10.1016/j.jag.2023.103534.

(12) Wu, W.; Liu, Y.; Rogers, B. M.; Xu, W.; Dong, Y.; Lu, W. Monitoring Gas Flaring in Texas Using Time-Series Sentinel-2 MSI and Landsat-8 OLI Images. *International Journal of Applied Earth Observation and Geoinformation* **2022**, *114*. https://doi.org/10.1016/j.jag.2022.103075.

(13) Dennison, P. E.; Matheson, D. S. Comparison of Fire Temperature and Fractional Area Modeled from SWIR, MIR, and TIR Multispectral and SWIR Hyperspectral Airborne Data. *Remote Sens. Environ.* **2011**, *115* (3), 876–886. https://doi.org/10.1016/j.rse.2010.11.015.

(14) Thorpe, A. K.; Green, R. O.; Thompson, D. R.; Brodrick, P. G.; Chapman, J. W.; Elder, C. D.; Irakulis-Loitxate, I.; Cusworth, D. H.; Ayasse, A. K.; Duren, R. M.; Frankenberg, C.; Guanter, L.; Worden, J. R.; Dennison, P. E.; Roberts, D. A.; Chadwick, K. D.; Eastwood, M. L.; Fahlen, J. E.; Miller, C. E. *Attribution of Individual Methane and Carbon Dioxide Emission Sources Using EMIT Observations from Space*; 2023. https://www.science.org.

(15) Asner, G. P. Carnegie Airborne Observatory: In-Flight Fusion of Hyperspectral Imaging and Waveform Light Detection and Ranging for Three-Dimensional Studies of Ecosystems. *J. Appl. Remote Sens.* **2007**, *1* (1). https://doi.org/10.1117/1.2794018.

(16) Ayasse, A. K.; Cusworth, D. H.; Howell, K.; O'Neill, K.; Conrad, B. M.; Johnson, M. R.; Heckler, J.; Asner, G. P.; Duren, R. Probability of Detection and Multi-Sensor Persistence of Methane Emissions from Coincident Airborne and Satellite Observations. *Environ. Sci. Technol.* **2024**. https://doi.org/10.1021/acs.est.4c06702.

(17) Dennison, P. E.; Roberts, D. A. Daytime Fire Detection Using Airborne Hyperspectral Data. *Remote Sens. Environ.* **2009**, *113* (8), 1646–1657. https://doi.org/10.1016/j.rse.2009.03.010.

(18) Elvidge, C. D.; Zhizhin, M.; Hsu, F. C.; Baugh, K. E. VIIRS Nightfire: Satellite Pyrometry at Night. *Remote Sens. (Basel).* **2013**, *5* (9), 4423–4449. https://doi.org/10.3390/rs5094423.

(19) Kim, J.; Cusworth, D. H.; Ayasse, A. K.; Howell, K.; O'Neill, K.; Duren, R. M. Performance of Airborne Imaging Spectrometers for Carbon Dioxide Detection and Emission Quantification. *Journal of Geophysical Research: Atmospheres* **2025**, *130* (7). https://doi.org/10.1029/2024JD042755.

(20) Conrad, B. M.; Tyner, D. R.; Johnson, M. R. Robust Probabilities of Detection and Quantification Uncertainty for Aerial Methane Detection: Examples for Three Airborne Technologies. *Remote Sens. Environ.* **2023**, *288*. https://doi.org/10.1016/j.rse.2023.113499.

(21) Willyard, K. A.; Schade, G. W. Flaring in Two Texas Shale Areas: Comparison of Bottom-up with Top-down Volume Estimates for 2012 to 2015. *Science of the Total Environment* **2019**, *691*, 243–251. https://doi.org/10.1016/j.scitotenv.2019.06.465.

(22) Seymour, S. P.; Aylward, B.; Galvin, K. P.; Kang, M.; Xie, D. Gas Flaring Is Likely Underestimated by Satellites Due to Undetected Small Flares. *Environ. Sci. Technol.* **2025**, *59* (40), 21465–21475. https://doi.org/10.1021/acs.est.5c03928.

(23) Plant, G.; Kort, E. A.; Brandt, A. R.; Chen, Y.; Fordice, G.; Gorchov Negron, A. M.; Schwietzke, S.; Smith, M.; Zavala-Araiza, D. Inefficient and Unlit Natural Gas Flares Both Emit Large Quantities of Methane. *Science (1979).* **2022**, *377* (6614), 1566–1571. https://doi.org/10.1126/science.abq0385.

(24) Brandt, A. R. Accuracy of Satellite-Derived Estimates of Flaring Volume for Offshore Oil and Gas Operations in Nine Countries. *Environmental Research Communications*. Institute of Physics 2020. https://doi.org/10.1088/2515-7620/ab8e17.

(25) *Dataset: 2012-2024 Flare Volume Estimates by Individual Flare Location*. https://thedocs.worldbank.org/en/doc/d01b4aebd8a10513c0e341de5e1f652e-0400072024/ related/2012-2023-individual-flare-volume-estimates.xlsx (accessed 2025-10-05).

(26) Duren, R.; Cusworth, D.; Ayasse, A.; Howell, K.; Diamond, A.; Scarpelli, T.; Kim, J.; O'neill, K.; Lai-Norling, J.; Thorpe, A.; Zandbergen, S. R.; Shaw, L.; Keremedjiev, M.; Guido, J.; Giuliano, P.; Goldstein, M.; Nallapu, R.; Barentsen, G.; Thompson, D. R.; Roth, K.; Jensen, D.; Eastwood, M.; Reuland, F.; Adams, T.; Brandt, A.; Kort, E. A.; Mason, J.; Green, R. O. The Carbon Mapper Emissions Monitoring System. *Atmos. Meas. Tech.* **2025**, *18* (22), 6933–6958. https://doi.org/10.5194/amt-18-6933-2025.

(27) Guanter, L.; Kaufmann, H.; Segl, K.; Foerster, S.; Rogass, C.; Chabrillat, S.; Kuester, T.; Hollstein, A.; Rossner, G.; Chlebek, C.; Straif, C.; Fischer, S.; Schrader, S.; Storch, T.; Heiden, U.; Mueller, A.; Bachmann, M.; Mühle, H.; Müller, R.; Habermeyer, M.; Ohndorf, A.; Hill, J.; Buddenbaum, H.; Hostert, P.; Van Der Linden, S.; Leitão, P. J.; Rabe, A.; Doerffer, R.; Krasemann, H.; Xi, H.; Mauser, W.; Hank, T.; Locherer, M.; Rast, M.; Staenz, K.; Sang, B. The EnMAP Spaceborne Imaging Spectroscopy Mission for Earth Observation. *Remote Sensing*. 2015. https://doi.org/10.3390/rs70708830.

(28) Loizzo, R.; Guarini, R.; Longo, F.; Scopa, T.; Formaro, R.; Facchinetti, C.; Varacalli, G. Prisma: The Italian Hyperspectral Mission. In *International Geoscience and Remote Sensing Symposium (IGARSS)*; 2018; Vol. 2018-July. https://doi.org/10.1109/IGARSS.2018.8518512.

(29) Cusworth, D. H.; Duren, R. M.; Ayasse, A. K.; Jiorle, R.; Howell, K.; Aubrey, A.; Green, R. O.; Eastwood, M. L.; Chapman, J. W.; Thorpe, A. K.; Heckler, J.; Asner, G. P.; Smith, M. L.; Thoma, E.; Krause, M. J.; Heins, D.; Thorneloe, S. *Quantifying Methane Emissions from United States Landfills*; 2024. https://www.science.org.

(30) Cusworth, D. H.; Duren, R. M.; Thorpe, A. K.; Olson-Duvall, W.; Heckler, J.; Chapman, J. W.; Eastwood, M. L.; Helmlinger, M. C.; Green, R. O.; Asner, G. P.; Dennison, P. E.; Miller, C. E. Intermittency of Large Methane Emitters in the Permian Basin. *Environ. Sci. Technol. Lett.* **2021**, *8* (7), 567–573. https://doi.org/10.1021/acs.estlett.1c00173.

(31) Duren, R. M.; Thorpe, A. K.; Foster, K. T.; Rafiq, T.; Hopkins, F. M.; Yadav, V.; Bue, B. D.; Thompson, D. R.; Conley, S.; Colombi, N. K.; Frankenberg, C.; McCubbin, I. B.; Eastwood, M. L.; Falk, M.; Herner, J. D.; Croes, B. E.; Green, R. O.; Miller, C. E. California's Methane Super-Emitters. *Nature* **2019**, *575* (7781), 180–184. https://doi.org/10.1038/s41586-019-1720-3.

(32) Frankenberg, C.; Thorpe, A. K.; Thompson, D. R.; Hulley, G.; Kort, E. A.; Vance, N.; Borchardt, J.; Krings, T.; Gerilowski, K.; Sweeney, C.; Conley, S.; Bue, B. D.; Aubrey, A. D.; Hook, S.; Green, R. O. Airborne Methane Remote Measurements Reveal Heavytail Flux Distribution in Four Corners Region. *Proceedings of the National Academy of Sciences* **2016**, *113* (35), 9734–9739. https://doi.org/10.1073/pnas.1605617113.

(33) Zhang, Z.; Cusworth, D. H.; Ayasse, A. K.; Sherwin, E. D.; Brandt, A. R. Measuring Carbon Dioxide Emissions From Liquefied Natural Gas (LNG) Terminals With Imaging Spectroscopy. *Geophys. Res. Lett.* **2023**, *50* (23). https://doi.org/10.1029/2023GL105755.

(34) Cusworth, D. H.; Thorpe, A. K.; Miller, C. E.; Ayasse, A. K.; Jiorle, R.; Duren, R. M.; Nassar, R.; Mastrogiacomo, J. P.; Nelson, R. R. Two Years of Satellite-Based Carbon Dioxide Emission Quantification at the World's Largest Coal-Fired Power Plants. *Atmos. Chem. Phys.* **2023**, *23* (22), 14577–14591. https://doi.org/10.5194/acp-23-14577-2023.

(35) Cusworth, D. H.; Duren, R. M.; Thorpe, A. K.; Eastwood, M. L.; Green, R. O.; Dennison, P. E.; Frankenberg, C.; Heckler, J. W.; Asner, G. P.; Miller, C. E. Quantifying Global Power Plant Carbon Dioxide Emissions With Imaging Spectroscopy. *AGU Advances* **2021**, *2* (2). https://doi.org/10.1029/2020av000350.

(36) Duren, R.; Gordon, D. Tackling Unlit and Inefficient Gas Flaring. *Science (1979).* **2022**, *377* (6614), 1486–11487. https://doi.org/10.3334/ORNLDAAC/1874.